

Article

Impact of Degree of Hydrophilicity of Pyridinium Bromide Derivatives on HCl Pickling of X-60 Mild Steel: Experimental and Theoretical Evaluations

Nurudeen A. Odewunmi ¹, Mohammad A. Jafar Mazumder ^{1,*}, Shaikh A. Ali ^{1,*},
Norah A. Aljeaban ², Bader G. Alharbi ², Abdulaziz A. Al-Saadi ¹ and Ime B. Obot ³

¹ Chemistry Department, King Fahd University of Petroleum and Minerals, Dhahran 31261, Saudi Arabia; nurudeen.odewunmi@kfupm.edu.sa (N.A.O.); asaadi@kfupm.edu.sa (A.A.A.-S.)

² EXPEC ARC, Saudi Aramco, Dhahran 31311, Saudi Arabia; norah.aljeaban@aramco.com (N.A.A.); bader.alharbi.1@aramco.com (B.G.A.)

³ Center of Research Excellence in Corrosion, Research Institute, King Fahd University of Petroleum and Minerals, Dhahran 31261, Saudi Arabia; obot@kfupm.edu.sa

* Correspondence: jafar@kfupm.edu.sa (M.A.J.M.); shaikh@kfupm.edu.sa (S.A.A.); Tel.: +966-13-8607836 (M.A.J.M.); +966-13-8607830 (S.A.A.)

Received: 27 December 2019; Accepted: 12 February 2020; Published: 19 February 2020



Abstract: Dodecyl pyridinium bromide (DDPB), tetradecyl pyridinium bromide (TDPB) and dodecyl 1,1'-bispyridinium dibromide (DDBPB) were successfully synthesized, characterized and evaluated for HCl pickling of X-60 low carbon steel. Order of corrosion inhibitions efficiencies, as revealed by both electrochemical and gravimetric studies, is TDPB > DDPB > DDBPB. The degree of hydrophilicity of inhibitors as predicted by a partition coefficient (Log P) and supported by a contact angle measurement was found to be responsible for their order of corrosion inhibition efficiencies. Adsorption of DDPB, TDPB, and DDBPB through the pyridinium nitrogen on mild steel surface was confirmed by ATR-FTIR and SEM-EDX analyses. The pyridinium nitrogen was found not to be the only factor responsible for their efficiency, but hydrophobes and the orientation of the hydrophilic ring were responsible, which incline to the deviation of experimental results and the order of Monte Carlo simulation adsorption energies. DDPB, TDPB, and DDBPB obey the Langmuir isotherm model despite major contributions of the film formed on the surface of X-60 mild steel on their overall inhibition corrosion resistance.

Keywords: pyridinium bromide derivatives; corrosion inhibitor; potentiodynamic polarization; electrochemical impedance; protective films; partition Coefficient; Monte Carlo simulation; acid pickling

1. Introduction

Effective elongation, high yield and tensile strength properties of X-60 low carbon steel (X-60 mild steel) as one of the API 5L grade X mild steel have made it a suitable metallic material in various offshore and onshore applications. These attractive mechanical properties, as well as its low cost compared to other alternative materials, have been a major consideration for its enormous applications despite poor resistance to corrosion in different environments [1–5]. Acid pickling is one of the important industrial processes where various acids are utilized for surface cleaning of metals. However, hydrochloric acid (HCl) pickling is preferred to other inorganic acids (hydrofluoric, sulfuric, phosphoric and nitric acids) pickling in steel mills and other steel applications industries due to its high regeneration, less pickling time, minimal loss of substrates, lower temperature and high-quality finished products [6,7]. To improve the economic importance of mild steel in pickling applications, corrosion inhibitors have been used to drastically reduce the effect of acid attack on mild steel [8–10].

Corrosion inhibitions of metals occur by either or both physical and chemical adsorptions of inhibitors on metal surfaces owing to the presence of heteroatom (sulphur, nitrogen, phosphorus and oxygen), multiple bonds and aromatic rings along with hydrophilic tails forming a protective film. Considerations of these features of corrosion inhibitors have led to the evaluations of numerous biological materials for effective corrosion inhibitors [11–18] due to their non-toxicity and biodegradable properties. Furthermore, novel ionic liquids [19–21] and some eco-friendly organic compounds containing different forms of functional groups, heteroaryl, aromatics cycles, saturated and unsaturated bonds in their molecular structures [22–27] have been reported as effective corrosion inhibitors.

Pyridinium salts are quaternary ammonium compounds that often made up of the hydrophilic part of a class of cationic surfactants that are mostly used as antibacterial, antimicrobial and biocidal agents [28–31]. However, it has been reported to be an important reagent for the development of novel organic compounds in catalysis [32–34], dialysis [35], thermoelectrical [36], drug delivery [37] and coatings applications [38]. Due to the presence of a hydrophilic center containing a nitrogen atom incorporated in a benzene ring, the ease of chemical integration of a suitable hydrophobic tail and halides (Cl^- or Br^-) to form suitable pyridinium salts, evaluation of its ability to perform as an effective corrosion inhibitor as halide salts, ionic compounds and synergistically with other compounds have been demonstrated [39–44].

The objective of this article is to synthesize three pyridinium bromide salts with modified hydrophobic tails and evaluate the effects of hydrophobic modifications on the corrosion inhibition efficiency on X-60 mild steel in 1 M HCl using gravimetric and electrochemical measurements. For this purpose, pyridinium bromide with 12-carbon chain hydrophobes: dodecyl pyridinium bromide (DDPB), 14-carbon chain hydrophobes: tetradecylpyridinium bromide (TDPB) and 12-carbon chain hydrophobes with two terminal hydrophilic centers: dodecyl 1,1'-bispyridinium dibromide (DDBPB) have been synthesized and evaluated as effective mild steel corrosion inhibitors in acidic media. This investigation would be complemented with surface analysis and Monte Carlo simulation to obtain strength of interaction of inhibitors with X-60 mild steel.

2. Experimental

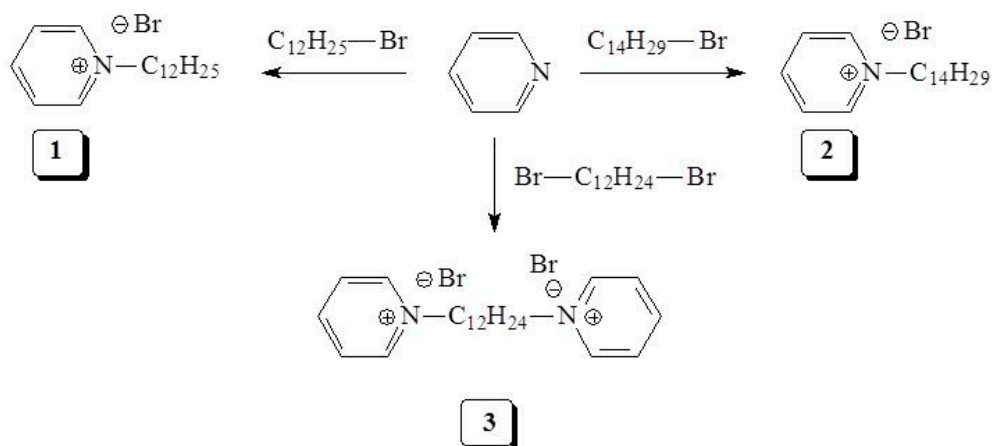
2.1. Materials

Unless and otherwise stated, all chemicals and solvents were purchased from Sigma Aldrich.

2.2. Synthesis

2.2.1. Synthesis of DPPB (1)

DDPB (1) was synthesized following the modified published procedure described elsewhere in the literature [45]; 1-bromododecane (20.1 g, 80.0 mmol) was added to a solution of pyridine (5.4 g, 68.0 mmol) in toluene at room temperature. The reaction mixture was then stirred under N_2 at 110 °C for 24 h. After the time elapsed, 50 mL of diethyl ether was added to the dense reaction mixture. The precipitate was decanted and redissolved in acetonitrile (20 mL). The crude product was then dropwise added to diethyl ether (100 mL). The precipitate was filtered to obtain the final product 1-*N*-dodecyl pyridinium bromide (1) as a white solid (Scheme 1) and dried in a vacuum at 50 °C for 6 h. Then, the product was removed from the vacuum oven and weighed to give a mass of 20.0 g, equivalent to a 92% yield.



Scheme 1. Synthesis route of dodecyl pyridinium bromide (DDPB) (1), tetradecylpyridinium bromide (TDPB) (2) and dodecyl 1,1'-bispyridinium dibromide (DDBPB) (3) corrosion inhibitors.

2.2.2. Synthesis of TDPB (2)

TDPB (2) was synthesized following the modified procedure described above. Briefly, 1-bromotetradecane (14.7 g, 53.3 mmol) was added to a solution of pyridine (3.6 g, 44.4 mmol) in toluene. The reaction mixture was then stirred under N_2 at $110\text{ }^\circ\text{C}$ for 24 h. After the time elapsed, diethyl ether was added to the dense reaction mixture. The precipitate was decanted and redissolved in acetonitrile (15 mL). The crude product was then dropwise added to diethyl ether (80 mL). The precipitate was filtered to obtain the final product 1-*N*-tetradecylpyridinium bromide (2) as a white solid (Scheme 1) and dried in a vacuum at $50\text{ }^\circ\text{C}$ for 6 h. Then, the product was removed from the vacuum oven and weighed to be 14.8 g corresponding to a 94% yield.

2.2.3. Synthesis of DDBPB (3)

DDBPB (3) was synthesized following the procedure described above. Briefly, 1,12-dibromododecane (8.01 g, 24.4 mmol) was added to a solution of pyridine (4.63 g, 58.5 mmol) in toluene at room temperature. The reaction mixture was then stirred under N_2 at $110\text{ }^\circ\text{C}$ for 24 h. After the time elapsed, the reaction mixture was cooled to room temperature during which phase separation occurred. The precipitate was redissolved in acetonitrile (15 mL) and reprecipitated in diethyl ether (80 mL). The precipitate was filtered to obtain the final product as a white solid, dodecyl 1,1'-bispyridinium dibromide (3) (Scheme 1) and dried in a vacuum at $50\text{ }^\circ\text{C}$ for 6 h. Then, the product was removed from the vacuum oven and weighed to be 8.97 g corresponding to a 76% yield.

2.3. Characterization of DDPB, TDPB and DDBPB

DDPB (1), TDPB (2) and DDBPB (3) were characterized by a melting point apparatus, elemental analyzer, FTIR, NMR and surface tensiometer. ^1H NMR and ^{13}C NMR were performed with a Bruker 400 MHz instrument (Bruker, Coventry, UK) while the FTIR spectra were obtained with PerkinElmer (16F PC FTIR) spectrometer (PerkinElmer, Waltham, MA, USA). Elemental analyses were carried out in a Carlo-Erba elemental analyzer (Carlo-Erba, model 1102, Waltham, MA, USA). Melting points were recorded in a calibrated Electrothermal-IA9100—Digital Melting Point Apparatus (Mettler Toledo, Columbus, OH, USA) using heating rates of $1\text{ }^\circ\text{C}/\text{min}$ in the vicinity of the melting points. The surface tension and critical micelle concentration (CMC) values for the pyridinium bromide derivatives DDPB, TDPB and DDBPB were measured in 1 M HCl using a surface tensiometer (PHYWE, Gottingen, Germany) by the du Nouy ring method [46].

2.4. Corrosion Studies

2.4.1. Material Preparation

The chemical composition of the low carbon steel (X-60) used for this investigation has been reported to contain above 96% Fe content [2]. It was cut into coupons of dimension $3 \times 3 \times 1 \text{ cm}^3$ in preparation for gravimetric and electrochemical measurements. Before corrosion studies, silicon carbide paper of different abrasive grades numbers (#120–#1000) were used successively to grind the surface of the coupons. After grinding, residues were removed by rinsing with distilled water, degreased by sonication in ethanol bath for 10 min, rinsed with acetone, dried with warm air and stored in the desiccator before use. A 1 M HCl corrosive acidic medium was prepared by dilution with distilled water from 37% purity analytical grade concentrated HCl. Stock solutions of synthesized DDPB (1), TDPB (2) and DDBPB (3) corrosion inhibitors were prepared in 1 M HCl from which corresponding volumes of aliquot were used to prepare the desired concentration range that was the selected base of experimental optimization of 5–50 mg/L by dilution.

2.4.2. Gravimetric Study

Gravimetric measurements were performed using the guidelines obtained from ASTM G 1–03 standard procedures for evaluating, cleaning and preparing mild steel coupons [47]. Coupons were weighed and completely immersed by suspension with the aid of a thread into a Wheaton glass bottle containing 1 M HCl solutions in the absence and presence of different concentrations of DDPB, TDPB and DDBPB. The temperature of the testing solution was maintained at 25 °C, 45 °C and 60 °C with the aid of a thermostated water bath for 24 h. After the time elapsed, the coupon was removed and placed in Clarke's solution for about 120 s to loosen the corrosion products. They were washed thoroughly with distilled water, rinsed with acetone, dried with a stream of warm air, allowed to cool and reweighed to determine the weight loss.

2.4.3. Electrochemical Study

Electrochemical studies were undertaken with a three-electrode system in an electrochemical cell designed for varieties of flat samples at 25 °C with an exposed area of 1 cm^2 . Graphite rod was used as a counter electrode, saturated calomel electrode (SCE) as a reference electrode and X-60 mild steel coupon as a working electrode. The electrochemical cell was connected to Gamry Potentiostat/Galvanostat/ZRA (reference PC14750-37058) incorporated with the Gamry ESA410 framework system. The framework system comprises of EIS300 software used for electrochemical impedance measurement, and D105corrosion software used for both linear polarization resistance and potentiodynamic polarization measurements. Gamry Echem Analyst software was utilized for data fittings of the electrochemical impedance measurements. The frequency range of 100 KHz and 10 mHz with an amplitude of 10 mV was used in the impedance measurements. Linear polarization resistance experiments were conducted by polarizing the working electrode with +10 and –10 mV potential against the corrosion potential (E_{corr}) with a scan rate of 0.125 mV/s. Curves of potentiodynamic polarization experiments were obtained by setting the instrument to apply –250 mV as the cathodic potential and +250 mV as the anodic potential relative to the corrosion potential (E_{corr}) with a scan rate of 0.5 mV/s. This condition will enable the cathodic and anodic curves to run consecutively. Corrosion current densities (I_{corr}) along with other interesting electrochemical parameters were extrapolated from the linear Tafel region of the anodic and cathodic segments of the curve against the corrosion potential.

2.5. Monte Carlo Simulation and Partition Coefficient (Log P)

Monte Carlo simulation was carried out using the Adsorption Locator module in Material Studio 7.0 software licensed from Accelrys Inc. USA. Low configuration adsorption energy for the interactions of DDPB, TDPB and DDBPB on Fe (110) surface in the aqueous phase was computed. Universal force field (UFF) was used to optimize structures of DDPB, TDPB and DDBPB and other components of

the system. The MC calculation of the simulation of the interaction between the inhibitor molecules and Fe(110) surface was carried out with a slab thickness of a 5 Å simulation box, which was enlarged to (10 × 10) a supercell with a vacuum slab of 50 Å to accommodate 30 molecules of water added to mimic a corrosion environment in reality. Partition coefficient (Log P) properties of DDPB, TDPB and DDBPB in solution were predicted with ACD/LABS Percepta licensed software.

2.6. Surface Analysis

A contact angle instrument integrated with an Attension Theta Optical Tensiometer (Biolin Scientific, Espoo, Finland) was utilized to evaluate the hydrophilicity of the protective film formed on X-60 mild steel by inhibitors. Measurements were carried out at an average of 6 locations with a water droplet of ~25 µL on the coupon after complete immersion for 24 h in the presence of an optimum concentration of inhibitors at 25 °C. The sessile drop technique was used to calculate the right and left angle of the droplet.

Adsorption of inhibitors on the substrates was confirmed with Thermo Nicolet 6700 FTIR spectrometer (Thermo Scientific, Fishers, IN, USA) with Smart Orbit diamond micro-ATR. After background correction, a total of 16 scans was performed between 500 and 4000 cm⁻¹ for identifications of functional groups of inhibitors on the mild steel coupons.

Surface morphologies of coupons in the absence and presence of 30 mg/L inhibitors were evaluated with a scanning electron microscope (SEM Emcrafts Genesis-2120 series, Gyeonggi-do, Korea), integrated with an energy dispersive x-ray spectrometer (EDX, Oxford Inc., Abingdon, UK). Before the exposure of coupons to different testing solutions, they were further polished with a cloth containing 1 µm of diamond paste to obtain a near mirror surface after the regular silicon carbide paper of different abrasive grade numbers (#120–#1000) grinding. Coupons were retrieved after 24 h, rinsed with distilled water, dried and SEM analysis was immediately performed.

3. Results and Discussions

3.1. Characterization of Synthesized DDPB, TDPB and DDBPB

¹H NMR, ¹³C NMR and FTIR spectra obtained for DDPB, TDPB and DDBPB are presented as Figures S1–S3, respectively.

DDPB (1): The onset of thermal decomposition (closed capillary): the color change to brown at 152.4 °C, indicating the melting point of DDPB. Elemental analysis for the molecular formula C₁₇H₃₀NBr calculated: C, 58.6; H, 9.3; N, 4.0; found: C, 58.9; H, 9.4; N, 3.9. FTIR: ν_{max} (neat): 3402, 3060 (pyridine, CH stretching), 2918, 2852 (aliphatic, C_{sp3}-H stretching), 1635 (C=N stretching), 1482 (C-H stretching), 1323, 1172 (aromatic C-H bending), 1037, 777, and 679 cm⁻¹. ¹H NMR: δ_H (CDCl₃) 0.86 (3H, t), 1.22–1.34 (18H, m), 2.03 (2H, q), 4.98 (2H, q), 8.18 (2H, d), 8.54 (1H, t), 9.49 (2H, t) (TMS: 0.00 ppm). ¹³C NMR (CDCl₃): 14.0 (1C), 22.5 (1C), 25.9 (1C), 29.2 (7C), 31.8 (1C), 61.9 (1C), 128.4 (2C), 144.9 (1C), 145.2 (2C) (middle C in CDCl₃: 77.00).

TDPB (2): The melting point of TDPB (closed capillary) is indicated by the color change to brown at 159.2 °C. C₁₉H₃₄NBr elemental analysis calculated: C, 60.5; H, 9.6; N, 3.9; found: C, 60.6; H, 9.7; N, 3.7. FTIR: ν_{max} (neat): 3390, 3060 (pyridine, C-H stretching), 2916, 2851 (aliphatic, C_{sp3}-H stretching), 1634 (C=N stretching), 1482 (C-H stretching), 1368, 1323, 1172 (aromatic C-H bending), 1052, 778, and 679 cm⁻¹. ¹H NMR: δ_H (CDCl₃) 0.88 (3H, t), 1.23–1.35 (22H, m), 2.04 (2H, q), 4.99 (2H, q), 8.18 (2H, d), 8.54 (1H, t), 9.49 (2H, t) (TMS: 0.00 ppm). ¹³C NMR (CDCl₃): 14.0 (1C), 22.6 (1C), 25.9 (1C), 29.5 (9C), 31.8 (1C), 62.1 (1C), 128.4 (2C), 144.9 (1C), 145.2 (2C) (middle C in CDCl₃: 77.00).

DDBPB (3): The onset of thermal decomposition (closed capillary): the color changed to brown at 167.3 °C, indicating the melting point of DDBPB. Elemental analysis of DDBPB (3) with a molecular formula C₂₂H₃₄N₂Br₂ calculated: C, 54.33; H, 7.05; N, 5.76; found: C, 54.41; H, 7.15; N, 5.87. FTIR: ν_{max} (neat): 3361, 3016 (pyridine, CH stretching), 2924, 2847 (aliphatic, C_{sp3}-H stretching), 2359, 1622

(C=N stretching), 1479 (C-H stretching), 1320, 1203, 1159 (aromatic C-H bending), 1055, 787, 773, and 687 cm^{-1} . ^1H NMR: δ_{H} (CDCl_3) 1.06-1.25 (16H, m), 1.96 (4H, m), 4.94 (4H, t), 8.15 (4H, t), 8.64 (2H, t), 9.56 (4H, t) (TMS: 0.00 ppm). ^{13}C NMR (CDCl_3): 25.8 (2C), 29.1(6C), 32.0 (2C), 61.6 (2C), 128.6 (4C), 145.0 (4C), 145.7 (2C) (middle C in CDCl_3 : 77.00).

3.2. Gravimetric Study

An average value of triplicate measurements of the weight losses was used to compute inhibition efficiency (E_w) and corrosion rate (C_R) using Equations (1) and (2), respectively.

$$E_w = \frac{\Delta W}{W_{\text{blank}}} \times 100 \quad (1)$$

$$C_R \text{ (mm/yr)} = \frac{87600 \times \Delta W}{\rho AT} \quad (2)$$

where ΔW is the average weight loss (g) between weight loss in the absence of inhibitor (W_{blank}) and in the presence of inhibitors, ρ is the density of steel (mainly Fe) taken as 7.86 g/cm^3 , A is the surface area of the coupon immersed, which computes as $A = 2(lw + lh + wh)$ for the length (l), width (w) and height (h) of the coupon, and T is the immersion time (h).

Figure 1a,b show corrosion inhibition efficiency and corrosion rate of different concentrations of DDPB, TDPB and DDBPB, respectively. The inhibition efficiency was found to increase while corrosion rates were found to decrease at 25°C as the concentration of inhibitors (DDPB, TDPB and DDBPB) increases from 5–30 mg/L in a similar pattern but at different rates. This is an indication that DDPB, TDPB and DDBPB effectively retard dissolution of X-60 mild steel in 1 M HCl solution when compared with the blank (absence of inhibitor). However, a further increase in concentration to 50 mg/L resulted in lower efficiency. This behavior can be attributed to the attainment of optimum coverage of all inhibitors at 30 mg/L and the possibility of additional concentration of inhibitors unadsorbed on the metal surface tends to interact with the adsorbed inhibitor and thereby causing desorption of the adsorbed molecule with the consequence of reduced inhibition efficiency. A similar kind of behavior for a particular corrosion inhibitor in different concentrations has been reported in the literature [48]. Surprisingly, TDPB E_w was observed to be about 90.9%, while DDPB and DDBPB achieved 87.1% and 79.4%, respectively, making order of corrosion mitigation effectiveness to be TDPB > DDPB > DDBPB for the gravimetric study at 25°C .

The surface tension versus inhibitor concentration profile was constructed to find the pyridinium bromide salt's CMC, which can be used to compare the adsorption pattern on either side of the CMC. Considering the molar concentration of corrosion inhibitors (converted to mg/L), the CMC, as well as surface tension of the pyridinium bromide salts, are found to follow the orders: DDBPB > DDPB > TDPB (Table S1). In 1 M HCl solution, the bispyridinium derivatives DDBPB, having pyridinium hydrophilic polar heads, are expected to have greater CMC values for being more soluble in water than its 12C and 14C hydrophobic pyridinium counterparts. The increase in the hydrophobic alkyl chain length decreases the solubility of the pyridinium bromide derivatives and, as expected, decreases the CMC [46]. The CMC values (Figure S4, Table S1) and the surface coverage (θ) data (Figure 1a) suggested that pyridinium bromide derivatives cover most of the mild steel surface before the concentrations reach their CMC values. The standard free energy of micelle formation ($\Delta G^\circ_{\text{mic}}$) of DDPB, TDPB and DDBPB can be calculated from Equation (3),

$$\Delta G^\circ_{\text{mic}} = RT \ln(C_{\text{cmc}}) \quad (3)$$

where R , T and C_{cmc} represent the gas constant, temperature and concentration in molL^{-1} of the pyridinium bromide salt at the CMC.

It was found that the adsorption on the metal surface is favored over the micellization since the $\Delta G^\circ_{\text{ads}}$ values (vide infra) are more negative (Table S2) compared with the corresponding $\Delta G^\circ_{\text{mic}}$

(Table S1). The monolayer formation at the interface between the metal and solution is complete before the CMC, after which multilayer coverage due to the adsorption of the micelles may impart further protection, albeit to a lesser degree [49].

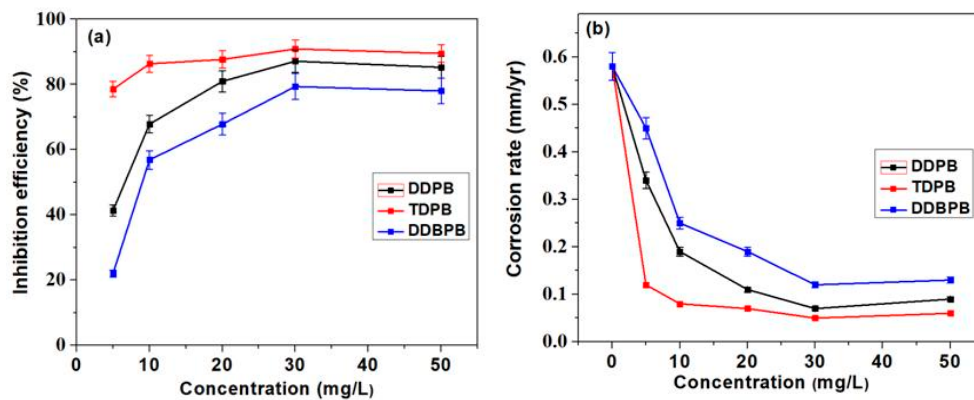


Figure 1. (a) Inhibition efficiency and (b) corrosion rate variations of X-60 mild steel in absence and presence of different concentrations of DDPB, TDPB and DDBPB from gravimetric measurement for 24 h immersion time in 1 M HCl solution at 25 °C.

The effects of temperature on the optimum concentration (30 mg/L) of inhibitors were investigated and presented as Figure 2. Figure 2a,b depicts the effect of temperature on inhibition efficiency and corrosion rate inhibitors from 25 to 60 °C, respectively. The efficiency of all inhibitors was observed to reduce at elevated temperature, indicating that thermal agitation increases the dissolution rate of X-60 mild steel in the corrosive medium. The effect of temperature was found to be relatively severe on DDBPB due to a large decrease in inhibition efficiency (Figure 2a) and a large increase in corrosion rate (Figure 2b) as a result of the greater effect of thermal agitation of DDBPB molecule on the mild steel surface. However, TDPB and DDPB were not affected much by increasing temperature. The superiority of TDPB was obvious in Figure 2a,b for the inhibition efficiency and corrosion rate variations comparisons between inhibitors at 25 °C, 45 °C and 60 °C, respectively. TDPB was found to achieve the highest E_w (Figure 2a) and the lowest corrosion rate (Figure 2b) in all investigated temperatures, indicating that the order of inhibitors effectiveness (TDPB > DDPB > DDBPB) on X-60 mild steel in 1 M HCl is the same for 25 °C, 45 °C and 60 °C.

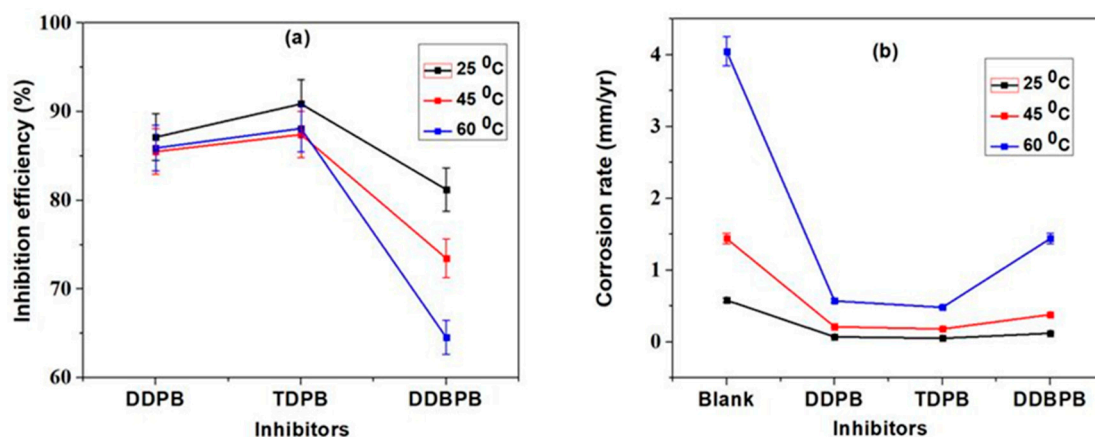


Figure 2. Gravimetric measurement for 24 h immersion time of 30 mg/L of DDPB, TDPB and DDBPB X-60 mild steel in 1 M HCl solution at different temperatures; (a) inhibition efficiency and (b) corrosion rate at 25 °C, 45 °C and 60 °C.

3.3. Electrochemical Evaluation

3.3.1. Impedance Measurements

All electrochemical measurements were recorded after 1 h immersion time of X-60 mild steel in the testing solution in the absence and presence of inhibitors to ensure a stable open circuit potential (OCP), as shown in Figure 3. The direction of potential change about the blank solution is a function of how the electrical double layer adjusts to accommodate the electrolyte system. It can be observed that potential in the different concentrations of DDPB, TDPB and DDBPB was either stable or increasing but later decreasing compared with the blank, suggesting the breaking down of a film before stabilization. This can be attributed to the bulky nature of DDPB, TDPB and DDBPB forming a porous film on X-60 mild steel surface that will contribute to slowing down the rate of corrosion. The slight shift in the potential in the presence of an inhibitor suggests both an anodic and cathodic mechanism of protection.

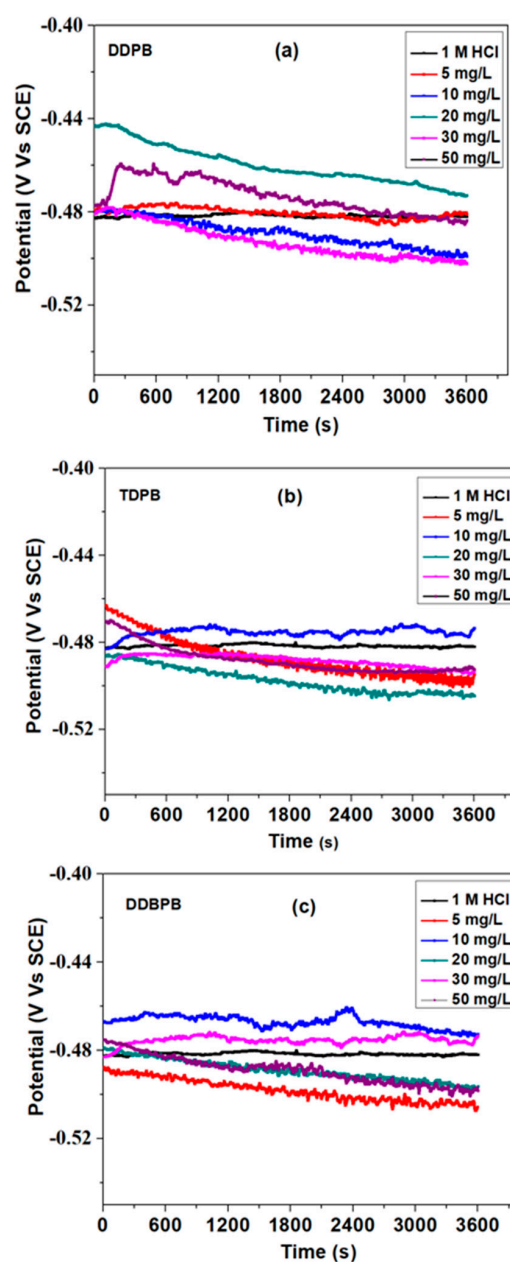


Figure 3. Open circuit potential plots for X-60 mild steel in 1 M HCl solution at 25 °C in the absence and presence of (a) DDPB, (b) TDPB and (c) DDBPB.

To characterize the capacitive behaviors and kinetics of the electrochemical process of DDPB, TDPB and DDBPB on X-60 mild steel surface, an impedance measurement was carried out after 1 h of OCP. Nyquist and Bode's (modulus and phase angle) plots of DDPB, TDPB and DDBPB are presented in Figures 4 and 5, respectively, for better comparison. It can be observed in the Nyquist plots (Figure 4) that the real impedance values increase as the concentration of DDPB, TDPB and DDBPB increases, as indicated by the corresponding diameters. TDPB (Figure 4b) was found to have the maximum real impedance value followed by DDPB (Figure 4a) and DDBPB (Figure 4c) at 30 mg/L concentrations with lower values for all inhibitors at 50 mg/L concentrations. This behavior is in agreement with what was observed in the gravimetric measurement for DDPB, TDPB and DDBPB. Exhibition of a single semi-circle with no shoulder, indicating a relaxation process [50,51], can be observed in the absence of DDPB, TDPB and DDBPB, but the presence of different concentrations of DDPB, TDPB and DDBPB introduced a shoulder on the semi-circle, indicating an additional relaxation process, suggesting a double relaxation process as a result of film formation on the X-60 mild steel surface. The extent of the interaction of DDPB, TDPB and DDBPB with X-60 mild steel in the testing medium can be easily predicted by the shape exhibited by the individual inhibitor on the Bode's plots (Figure 5). Curves close to a straight line between the solution resistance and the total resistance can be observed in the modulus plots (Figure 5e), and non-distinguishable minimal deflections similar to the blank in the phase angle plots (Figure 5f) for DDBPB are a relative indication of the least interaction of DDBPB with X-60 mild steel. Moderate interaction can be suggested for DDPB comparing the non-linearity of the curve of the modulus plot (Figure 5a) and a broader distinguishable minimal deflections phase angle (Figure 5b) clearly showing the existence of two times constant. However, it is obvious from the curve exhibited in the modulus plots (Figure 5c) and the glaring two minimal deflections in the phase angle plots (Figure 5d) for TDPB showing a superiority interaction of TDPB in agreement with the claimed order of effectiveness (TDPB > DDPB > DDBPB), conforming with their extent of interaction with X-60 mild steel.

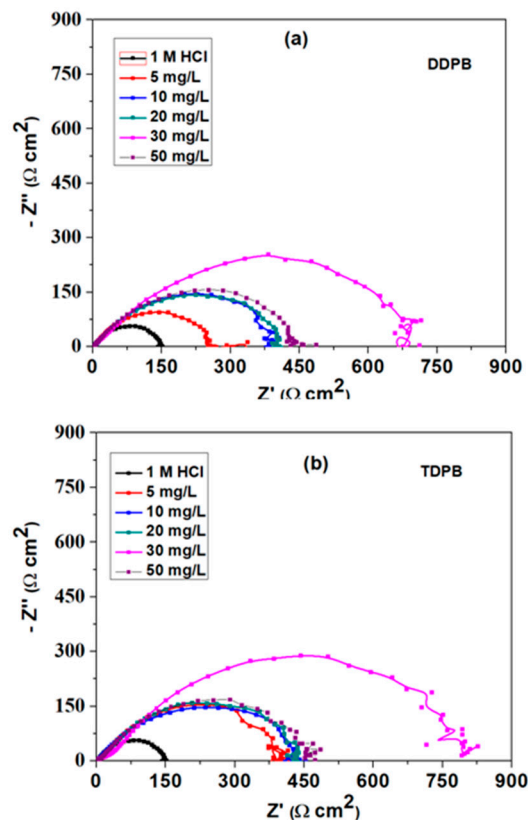


Figure 4. Cont.

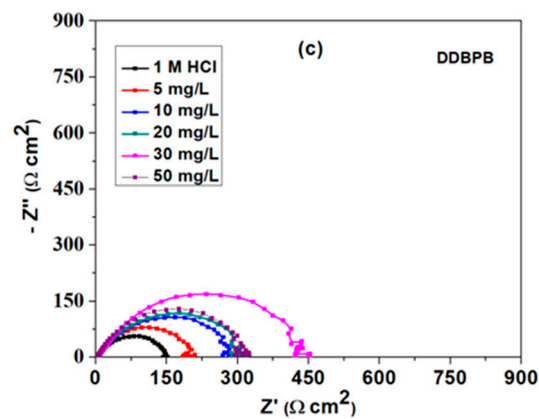


Figure 4. Nyquist plots for X-60 mild steel in 1 M HCl solution at 25 °C in the absence and presence of different concentrations of (a) DDPB, (b) TDPB and (c) DDBPB.

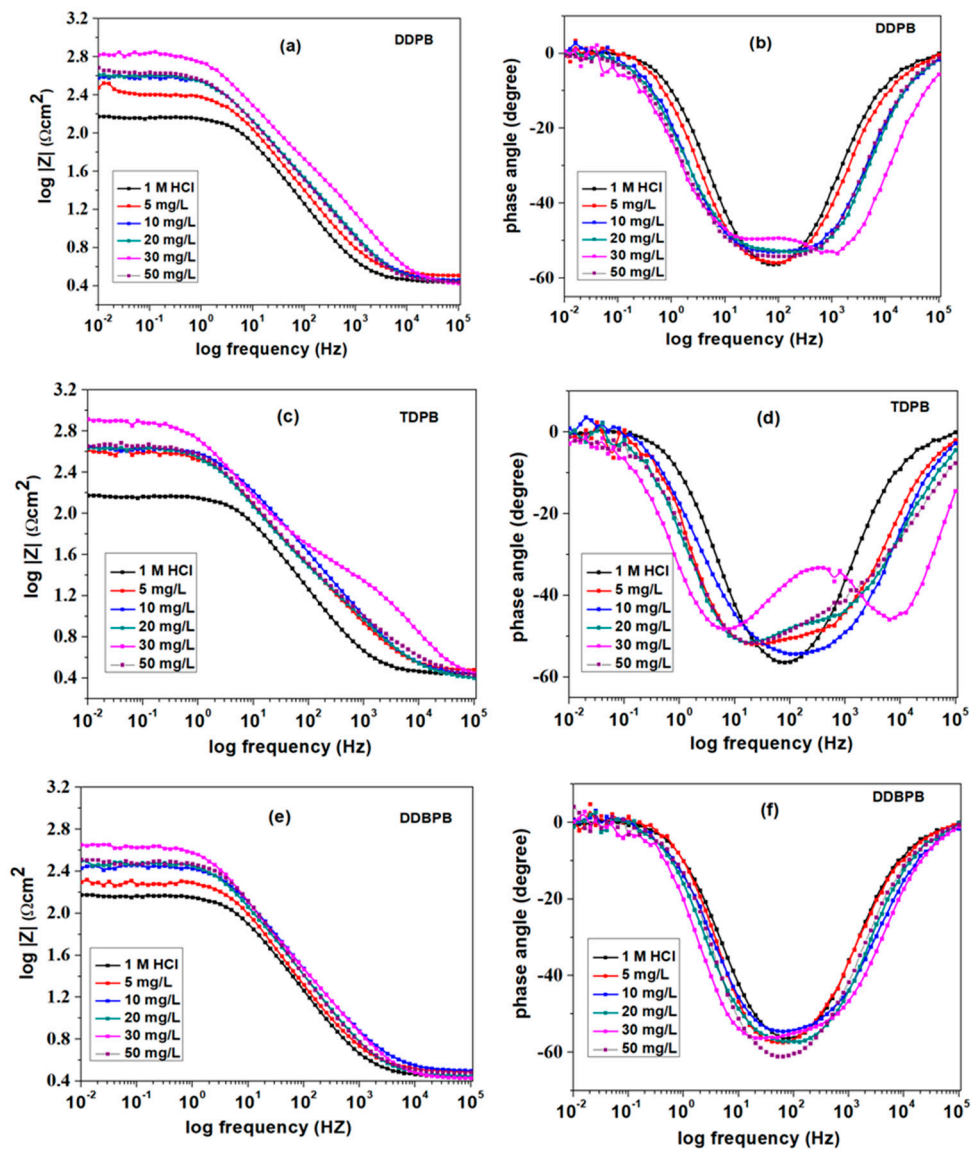


Figure 5. Bode plots for X-60 mild steel in 1 M HCl solution at 25 °C in the absence and presence of different concentrations of (a,b) DDPB, (c,d) TDPB and (e,f) DDBPB modulus and phase angle, respectively.

Modeling a suitable electrical equivalent circuit to generate data for the impedance plots requires considering shapes of the Nyquist semicircle, curves of modulus plots and nature of deflections in the phase angle plots. The imperfect semicircle of the Nyquist plot and minimal deflection point of angle lower than 90° suggest the relaxation porosity effect due to surface roughness, mass transfer, non-homogeneity of local dielectric material and time constant frequency dispersion [52], which can be accounted for by the introduction of a constant phase element [53] in place of capacitance in the equivalent circuit. Also, numbers of distinguishable maxima or minimal deflections related to shoulders indicated by the modulus phase angle plot are equivalent to numbers of the time constant of the electrochemical system processes [51].

Reliable chi-square (χ^2) fitting values were obtained using Figure 6a,b to fit impedance plots in the absence and presence of DDPB, TDPB and DDBPB, respectively. Electrochemical impedance parameters are listed in Table 1 along with other estimated data for X-60 mild steel in the absence and presence of DDPB, TDPB and DDBPB. Impedance efficiency (E_{imp}) is estimated by computing the percentage difference between the total charge transfer resistance in the presence (R_T) and absence (R_{ct^0}) of DDPB, TDPB and DDBPB, as shown in Equations (4) and (5).

$$R_T = R_f + R_{ct} \tag{4}$$

$$E_{imp}(\%) = \frac{R_T - R_{ct^0}}{R_T} \times 100 \tag{5}$$

where R_T is the total resistance comprised of the charge transfer resistance of the film (R_f) and the charge transfer resistance of the double layer in the presence (R_{ct}) and absence (R_{ct^0}) of DDPB, TDPB and DDBPB.

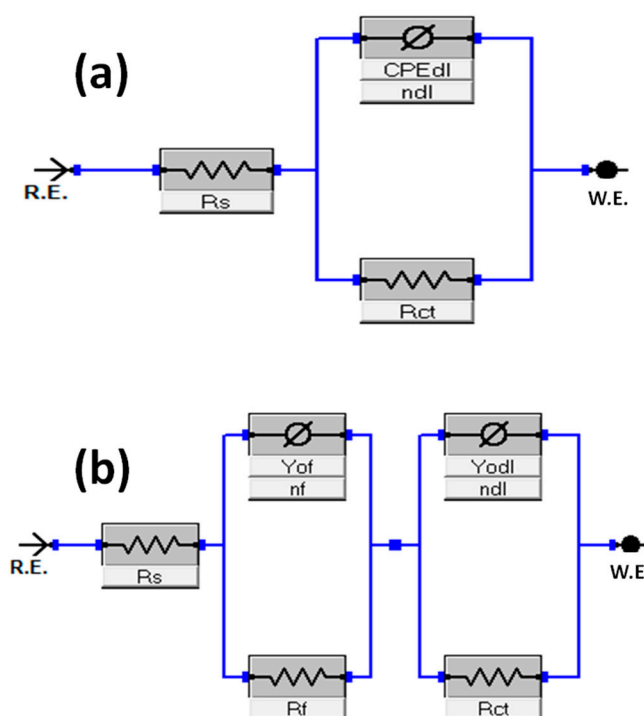


Figure 6. Equivalent circuit diagrams for impedance data fittings in 1 M HCl solution in the (a) absence and (b) presence of DDPB, TDPB and DDBPB.

Table 1. Impedance parameters of X-60 mild steel in the absence and presence of different concentrations of DDPB, TDPB and DDBPB at 25 °C.

Inhibitor	Conc. (mg/L)	R_s (Ωcm^2)	CPE _f		CPE _{dl}			R_T (Ωcm^2)	$\chi^2 \times 10^{-3}$	E_{imp} (%)	
			Y_{of} ($\mu\Omega\text{S}^n/\text{cm}^2$)	n_f	R_f (Ωcm^2)	Y_{odl} ($\mu\Omega\text{S}^n/\text{cm}^2$)	n_{dl}				R_{ct} (Ωcm^2)
DDPB	Blank	2.75	-	-	-	342.9	0.79	148.0	148.0	0.69	-
	5	3.13	330.1	0.75	240.4	979.1	1.10	26.5	266.9	2.28	44.5
	10	2.79	235.1	0.84	362.5	370.6	0.74	28.2	390.7	0.71	62.1
	20	2.69	260.9	0.80	387.3	295.8	0.78	19.7	407.0	0.52	63.6
	30	2.53	199.2	0.78	666.1	131.0	0.78	30.4	696.5	0.99	78.8
	50	2.70	279.4	0.79	429.5	364.9	0.79	16.7	446.2	0.48	66.8
TDPB	5	2.86	250.3	0.86	366.6	414.4	0.70	29.9	396.5	0.96	62.7
	10	2.63	211.7	0.82	385.7	419.9	0.70	43.5	429.2	1.12	65.5
	20	2.36	291.6	0.82	414.5	536.6	0.65	24.4	438.9	0.46	66.3
	30	2.25	309.2	0.75	798.0	50.7	0.75	28.6	826.6	1.52	82.1
	50	2.23	1098.0	0.54	188.1	328.6	0.93	284.1	472.2	0.46	68.7
DDBPB	5	3.05	747.5	0.71	35.3	215.4	0.96	156.5	191.8	0.91	22.8
	10	3.06	203.4	0.87	254.7	563.6	0.71	24.3	279.0	0.73	47.0
	20	2.73	461.5	0.74	52.4	241.4	0.93	245.4	297.8	0.70	50.3
	30	2.47	412.0	0.69	284.4	335.1	1.11	156.0	440.4	1.47	66.4
	50	2.96	175.5	0.93	272.1	762.4	0.71	36.2	308.3	0.62	52.0

It can also be observed that the percentage efficiency of all inhibitors increases with an increase in concentration from 5 mg/L up to the optimum values of 30 mg/L, with a further increase in concentration decrease efficiency of all inhibitors. The efficiency of 78.8%, 82.1% and 66.4% were achieved for DDPB, TDPB and DDBPB, respectively, in the same order of superiority from the gravimetric experiment. Furthermore, it was found that resistance of the film (R_f) as a result of a protective film formation by DDPB, TDPB and DDBPB plays a major role in the total resistance (R_T). Effective corrosion inhibition of DDPB, TDPB and DDBPB could be attributed to the adsorption of the pie bond of the aromatic and the ionized quaternary pyridimic nitrogen on the X-60 mild steel forming a protective film with the hydrophobes, thereby creating a barrier for charge and mass transfer to isolate corroding ion from attacking X-60 mild steel.

3.3.2. Polarization Measurements

A direct current approach by potentiodynamic polarization (PDP) technique was used to gain insight into the change in the kinetics of cathodic and anodic reactions of X-60 mild steel in 1 M HCl in the presence of DDPB, TDPB and DDBPB. Tafel curves generated from the PDP measurements were presented in Figure 7. It can be observed that all curves exhibit similar nature of polarization in both directions but characterized with lower current density cathodic and anodic regions in the presence of different concentrations of DDPB, TDPB and DDBPB when compared with the anodic and cathodic curves of the X-60 mild steel in the absence of an inhibitor. This behavior characterized by a reduction in current density in the anodic and cathodic direction of the Tafel curve is an indication of a mixed-type corrosion inhibition mechanism. However, the extent of reduction of the current density was found to depend on the type of inhibitor (DDPB, TDPB or DDBPB) present in the testing medium. Tafel anodic slopes (β_a), cathodic slopes (β_c), corrosion current densities (I_{corr}), corrosion potentials (E_{corr}) and corrosion rates (C_{rate}) extrapolated from the linear portion of the Tafel curves are enumerated in Table 2. A mixed type inhibitor (DDPB, TDPB and DDBPB) property can be further confirmed by the slight negative shift of E_{corr} in both directions and were observed in Table 2 when compared with the blank. Furthermore, corrosion rates of X-60 mild steel were found to decrease as the concentrations of DDPB, TDPB and DDBPB increase from 5 to 30 mg/L. Optimum concentrations of corrosion efficiency of DDPB, TDPB and DDBPB was found to be in good agreement with what was observed in the impedance and the gravimetric measurements. The percentage inhibition efficiencies (E_{pdp}) of inhibitors were computed using Equation (6) and listed in Table 2. Efficiencies of 83.3%, 88.0%

and 72.8% were achieved with 30 mg/L concentrations of DDPB, TDPB and DDBPB, respectively, following the order of superiority earlier observed from other techniques

$$E_{pdp} = \frac{I_{corr^{\circ}} - I_{corr}}{I_{corr^{\circ}}} \times 100 \quad (6)$$

where $I_{corr^{\circ}}$ and I_{corr} is the current density in absence and presence and of different concentrations of DDPB, TDPB and DDBPB, respectively.

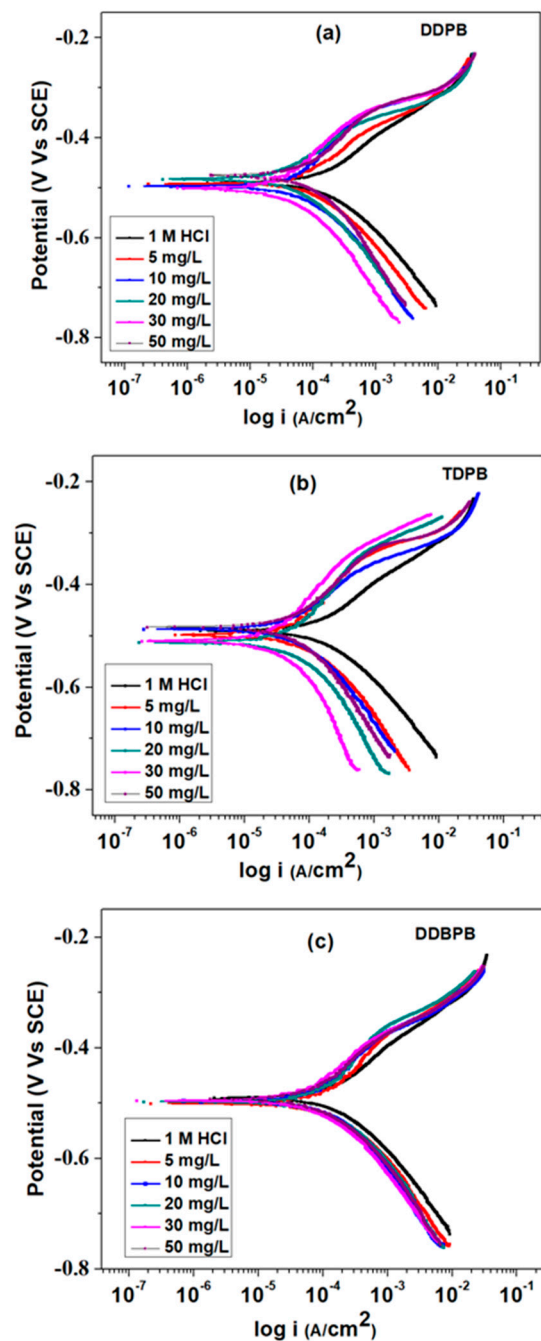


Figure 7. Potentiodynamic polarization plots of X-60 mild steel in 1 M HCl solution at 25 °C in the absence and presence of different concentrations of (a) DDPB, (b) TDPB and (c) DDBPB.

Table 2. Potentiodynamic polarization (PDP) and linear polarization resistance (LPR) parameters of X-60 mild steel in absence and presence of different concentrations of DDPB, TDPB and DDBPB at 25 °C.

Inhibitors	Conc. (mg/L)	PDP					LPR			
		E_{corr} (mV/SCE)	I_{corr} ($\mu\text{A}/\text{cm}^2$)	Crate (mm/yr)	β_a (mV/dec)	β_c (mV/dec)	E_{pdp} (%)	R_p (Ωcm^2)	Crate (mm/yr)	E_{lpr} (%)
DDPB	Blank	-490.0	167.0	76.50	124.1	118.1	-	161.6	73.6	-
	5	-492.0	94.8	43.32	196.1	79.80	43.2	315.4	34.9	48.8
	10	-497.0	65.1	29.74	151.8	141.8	61.0	344.7	33.4	53.1
	20	-483.0	47.8	21.84	109.2	132.3	71.4	494.1	23.8	67.3
	30	-501.1	27.9	12.76	109.5	87.7	83.3	623.9	18.3	74.1
	50	-475.0	70.1	32.04	99.7	100.9	58.0	509.0	19.0	68.3
TDPB	5	-497.0	63.4	28.9	159.5	114.4	62.2	410.9	28.8	60.7
	10	-487.0	57.7	26.4	120.4	124.6	65.5	445.3	26.2	63.7
	20	-513.0	58.0	26.5	172.4	123.9	65.5	545.0	21.3	70.4
	30	-510.0	20.1	9.2	106.9	90.6	88.0	853.6	13.7	81.1
	50	-482.0	74.6	34.1	144.4	179.8	55.3	431.9	23.4	62.6
DDBPB	5	-500.0	118.0	54.1	124.4	130.6	29.3	206.5	55.9	21.7
	10	-496.0	69.6	31.8	110.5	73.3	58.3	316.6	36.2	48.9
	20	-497.0	59.0	27.0	105.3	67.3	64.7	326.4	35.4	50.5
	30	-495.0	45.5	20.8	102.4	73.9	72.8	420.1	27.5	61.5
	50	-492.0	82.0	37.5	128.4	89.4	37.5	288.2	39.9	43.9

Corrosion rates and other electrochemical parameters obtained by linear polarization resistance (LPR) measurements in the absence and presence of different concentrations of DDPB, TDPB and DDBPB were also presented in Table 2. Polarization resistance (R_p) was obtained using the slopes of potential (E) versus current density (i) curves measured ± 10 mV at corrosion potential (E_{corr}). Inhibition efficiencies (E_{lpr}) of the LPR measurements were estimated by the percentage difference between the polarization resistance in the presence (R_p) and absence (R_{p°) of different concentrations of DDPB, TDPB and DDBPB using Equation (7).

$$E_{lpr}(\%) = \frac{R_p - R_{p^\circ}}{R_p} \times 100 \quad (7)$$

The corrosion rate was observed to decrease with an increase in concentration from 5–30 mg/L of DDPB, TDPB and DDBPB. Further increase in the concentration of inhibitors above 30 mg/L leads to an increase in corrosion rate and lower efficiency as evidenced by the presence of 50 mg/L concentrations for all inhibitors. This trend has been observed from other experimental techniques pointing towards 30 mg/L as the optimum concentration of DDPB, TDPB and DDBPB in the testing medium. Reduction in the corrosion rate of about 60.0, 55.3, and 46.1 mm/yr along with E_{lpr} of 81.1%, 74.1%, and 61.5% were achieved for 30 mg/L TDPB, DDPB and DDBPB, respectively, when compared with X-60 mild steel in the absence of inhibitors. The corrosion inhibition efficiencies results obtained for the polarization and impedance measurements are in close agreement with the gravimetric measurement.

3.4. Adsorption Isotherm

Adsorption isotherm was constructed to obtain information on the nature of adsorption of DDPB, TDPB and DDBPB on X-60 mild steel in HCl solution with an assumption of direct relationship between the degree of surface coverage (θ) and the inhibition efficiency of the impedance measurements ($\theta = E_{imp}/100$). This assumption is based on the fact that the extent of corrosion inhibition is a function of the surface condition of the substrate and nature of the adsorption of inhibitors. Different adsorption isotherm models were fitted with values obtained, but the Langmuir isotherm model was found to be

the best-fitted isotherm model base on correlation coefficient (R^2) values. It is a monolayer adsorption isotherm characterized by the expression presented as Equation (8):

$$\frac{C_{inh}}{\theta} = \frac{1}{K_{ads}} + C_{inh} \quad (8)$$

where θ is the surface coverage, C_{inh} is the concentration of DDPB, TDPB and DDBPB, and K_{ads} is the equilibrium constant of the adsorption process.

Plots of the ratio of concentrations (C) of DDPB, TDPB and DDBPB and surface coverage (θ) against concentrations (C) are presented as Figure S5, and parameters extrapolated from the model are enumerated in Table S2. It can be observed that slopes of 1.05, 1.10 and 0.99 obtained for DDPB, TDPB and DDBPB, respectively, are close to unity (1). This is an indication that all inhibitors obey the Langmuir isotherm model despite major contributions of the film formed on the surface of X-60 mild steel on their overall inhibition corrosion resistance. However, correlation efficiencies (R^2) values 0.990, 0.999 and 0.922 obtained for DDPB, TDPB and DDBPB, respectively, can be correlated to the extent of interaction of inhibitors revealed by impedance measurement.

Nature of adsorption of DDPB, TDPB and DDBPB on X-60 mild steel can be predicted from the K_{ads} that were obtained from the intercept of Langmuir plots by relating it with standard Gibbs free energy (ΔG_{ads}°) using Equation (9).

$$\Delta G_{ads}^\circ = -RT \ln \left(1 \times 10^6 K_{ads} \right) \quad (9)$$

where R is the universal gas constant, T is the absolute temperature in Kelvin and 1×10^6 is the concentration of water expressed in ppm (mg/L).

The physisorption process that is characterized by electrostatic interaction between the charged adsorbed molecule and the metal surface has been attributed to ΔG_{ads}° values of -20 kJ/mol or less, while the chemisorption process that is characterized by the formation of coordinate bond involving charge transfer or sharing between molecules of inhibitor and metal surface have been attributed to ΔG_{ads}° values of -40 kJ/mol or more [54]. Estimated values of ΔG_{ads}° enumerated in Table S2 are -38.1 , -33.3 and -40.3 kJ/mol for DDPB, TDPB and DDBPB, respectively. It can be deduced base on the ΔG_{ads}° values obtained that the adsorption process of DDPB, TDPB and DDBPB X-60 mild steel may involve both physisorption and chemisorption but more of the chemisorption process. These double adsorption processes can be explained by an assumption made by Lozano et al. [55] that there is likely an existence of strong adsorption of water molecule on X-60 mild steel surface, which will have more affinity for the ionized nitrogen center of the hydrophilic section of pyridinium bromide salt (physisorption process) and later accompanied by charge sharing or transfer between electron-rich centers of the inhibitor and the mild steel surface (chemisorption process) as a result of longer interaction time.

3.5. Monte Carlo Simulation and Log-P

The most stable energy configurations for the adsorption energy of DDPB, TDPB and DDBPB that were carried out in aqueous phase with 30 molecules of water to mimic corrosion environment snapshots are shown in Figure 8. It can be observed that the pyridinium ring is the center of adsorption for all Fe(110)/inhibitors systems. However, orientation of the aromatic ring of DDPB (Figure 8a) and TDPB (Figure 8b) are tilted in the same manner on the Fe(110) surface, while that of DDBPB (Figure 8c) is parallel with maximum contact on the Fe(110) surface and the other ring is tilted but does not have contact with the Fe(110) surface. It has been reported that the more negative adsorption energies of inhibitors are responsible for their degree of interactions with the metal surface and, thereby, proportional to their corrosion efficiencies [56]. Adsorption energies of -34.1 , -38.5 and -42.6 Kcal/mol computed for DDPB, TDPB and DDBPB, respectively, from the Monte Carlo simulation are shown in Table 3. The higher adsorption energy of TDPB than DDPB is in agreement with the experimental results. However, the highest adsorption energy of DDBPB when compared with both

TDPB and DDPB from the simulation study will distort the order of inhibition efficiencies (TDPB > DDPB > DDBPB) from the experimental results. Therefore, the rate of adsorptions of DDPB, TDPB and DDBPB on mild steel surface is likely not the only factor responsible for the order of their corrosion inhibition efficiencies.

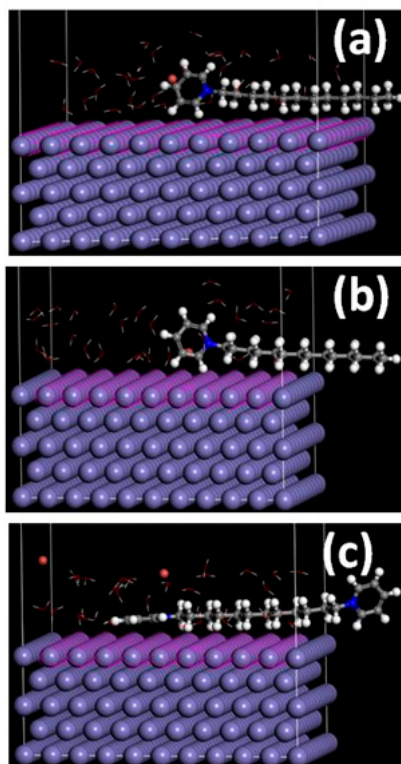


Figure 8. Most stable energy configurations of (a) DDPB, (b) TDPB and (c) DDBPB adsorptions on the Fe (110)/30 H₂O system by Monte Carlo simulation.

Table 3. Monte Carlo simulation's parameters for the adsorption of DDPB, TDPB and DDBPB on Fe (110)/30 H₂O interface.

Interface	Adsorption Energy of Inhibitors (Kcal/mol)	Adsorption Energy of H ₂ O (Kcal/mol)
Fe(110)/DDPB/30 H ₂ O	−34.1	−1.10
Fe(110)/TDPB/30 H ₂ O	−38.5	−1.24
Fe(110)/DDBPB/30 H ₂ O	−42.6	−1.22

Furthermore, degrees of solubility of DDPB, TDPB and DDBPB in solution were predicted with ACD/LLABS Percepta v.2018.1 software. Partition coefficient Log P ([organic]/[aqueous]) indicates the concentration of solute in an organic and aqueous partition. A negative value of Log P indicates a high affinity of the compound for the aqueous phase (more hydrophilic); Log P = 0 indicates equal partition of the compound between hydrophilic and hydrophobic phases; while a positive value indicates a highly hydrophobic phase. Values obtained were −0.03, 0.84 and −3.88 for DDPB, TDPB and DDBPB, respectively. It can be observed that TDPB has a positive value indicating a highly hydrophobic property of the protective film formed on X-60 mild steel, while DDPB is very close to zero, indicating a moderate hydrophobic property of the film. A very relatively high negative value of −3.88 was predicted for DDBPB. This indicates a high hydrophilic property of the film formed by DDBPB (most soluble). The degree of solubility of protective films formed on the surface of mild steel as predicted by Log P values (TDPB > DDPB > DDBPB) agrees with the order of inhibition efficiencies in the experimental results. Based on structural features of DDPB, TDPB and DDBPB, they can be classified as

surfactant corrosion inhibitors [57]. Corrosion inhibition efficiencies of surfactant corrosion inhibitors have been reported to depend not only on the adsorption energy parameter but include water and oil partition interaction along with several other factors [58].

3.6. Surface Analysis

FTIR-ATR was carried out to confirm the adsorptions of DDPB, TDPB and DDBPB on the surface of X-60 mild steel. FTIR-ATR spectra measurement was taken after 24 h immersion of X-60 in 1 M HCl in the presence of 30 mg/L DDPB, TDPB and DDBPB, and presented as Figure 9. Spectra of polished X-60 and X-60 in 1 M HCl are observed to be without any functional groups of inhibitors. However, all the functional groups of inhibitors presented in Figure S3 for DDPB, TDPB and DDBPB in pure forms are detected on the surface of mild steel in the presence of inhibitors. A broadening peak in the O-H band that is probably due to the moisture adsorbed by the pyridinium salts on mild steel surface in the corrosive environment can be observed between 3200 cm^{-1} and 3600 cm^{-1} . Doublet peaks of C-H stretch between 2800 cm^{-1} and 3000 cm^{-1} can also be observed on the surface of metals. Interactions of inhibitors with X-60 can be attributed to a slight shift in a position towards the left for C=N, C=C and aromatic in-plane bending observed at about 1600 cm^{-1} , 1300 cm^{-1} and 1000 cm^{-1} respectively. The presence of all these functional groups on the surface of mild steel confirmed that adsorption of DDPB, TDPB and DDBPB are responsible for the protection of X-60 mild steel in 1 M HCl.

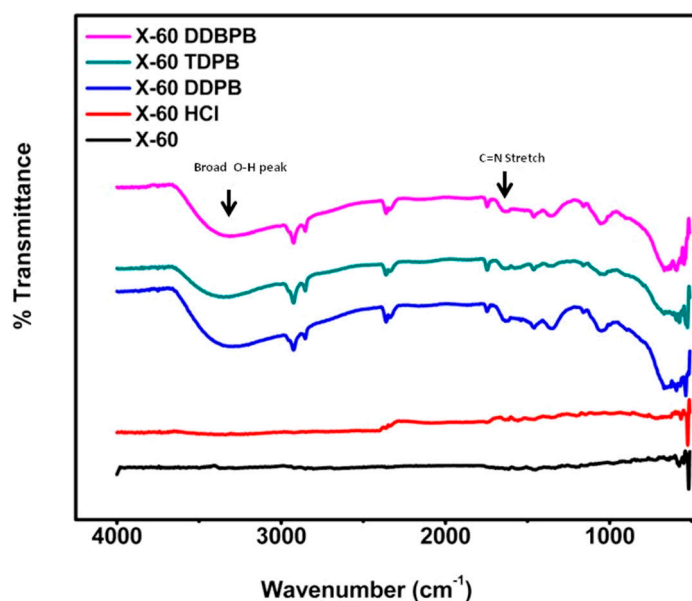


Figure 9. FTIR-ATR spectra showing adsorption of DDPB, TDPB and DDBPB on X-60 mild steel after complete immersion in the absence and presence of 30 mg/L inhibitors for 24 h at 25 °C.

Surface morphology studies (Figure 10) of X-60 mild steel coupons after 24 h exposure in 1 M HCl solution in the absence and presence of 30 mg/L of DDPB, TDPB and DDBPB at 25 °C were conducted by SEM to further confirm the adsorption of inhibitor on the mild steel surface. Comparing the image of polished X-60 mild steel without exposure to the testing solution shown in Figure 10a and the image after 24 h exposure in 1 M HCl solution (Figure 10b), a severe surface degradation was observed with very high surface roughness due to acid attack. The surface was observed to have undergone uniform corrosion with no evidence of localized corrosion. However, the surface roughness observed on the mild steel in Figure 10b was drastically reduced due to inhibiting effects of 30 mg/L inhibitors (DDPB, TDPB or DDBPB) in 1 M HCl solution on the metal surface, as shown in Figure 10c–e, respectively. Adsorption of inhibitors on the metal surface forming a protective layer against acid attack is responsible for the inhibition efficiency, as evidenced by the presence of adsorbate on the metal surface. EDX analysis spectra presented in Figure S6 revealed elemental compositions of X-60 mild

steel surface in the absence and presence of different inhibitors. The presence of trace amounts of a nitrogen atom in Figure S6c–e confirmed adsorptions of DDPB, TDPB and DDBPB on the X-60 surface.

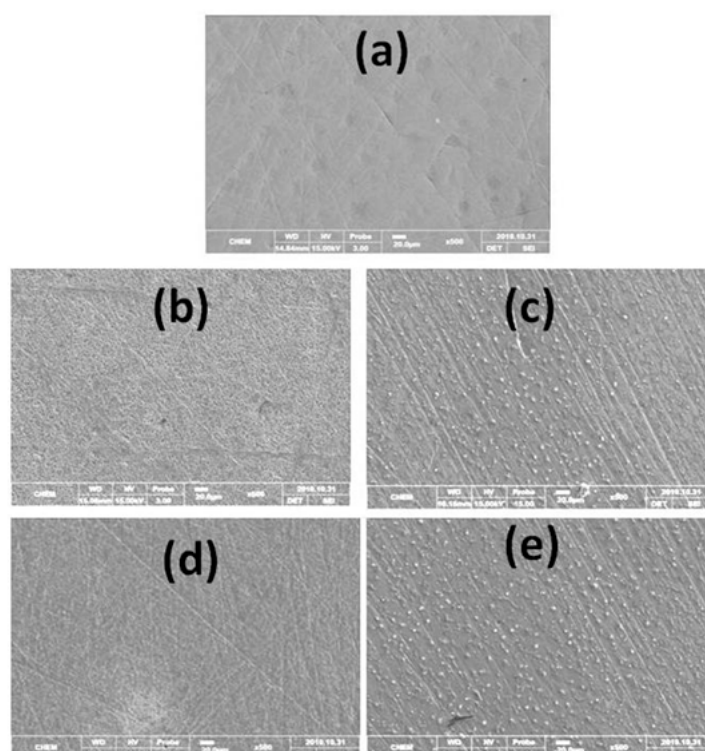


Figure 10. SEM images of X-60 mild steel in the absence and presence of 30 mg/L inhibitors after complete immersion in 1 M HCl for 24 h at 25 °C; (a) polished X-60 mild steel, (b) X-60 in 1 M HCl in the absence of inhibitor, and X-60 in 1 M HCl in the presence of (c) DDPB, (d) TDPB and (e) DDBPB.

The degree of hydrophilicity of the film formed on mild steel surface by DDPB, TDPB and DDBPB was investigated by contact angle measurements after immersion in the testing medium in the absence and presence of 30 mg/L inhibitors. A very obvious hydrophobic property of the polished X-60 mild steel coupon (Figure 11a) was established with a contact angle of an average of 101.4°. Immersion of X-60 sample in 1 M HCl solution for 24 h distorted the hydrophobic surface of the metal evidenced by the reduced contact angle with water droplet to 42.4° (Figure 11b) due to drastic acid attack. However, the effect of the acid attack was mitigated by the presence of DDPB, TDPB and DDBPB due to the formation of a protective film on the X-60 surface with improved contact angle values of different magnitudes. Average contact angles measured, as shown in Figure 11c–e, are 58.9°, 75.8° and 47.1° for DDPB, TDPB and DDBPB, respectively. The order of magnitude of the contact angle shows that TDPB > DDPB > DDBPB, which indicates a decrease in hydrophilicity of the protecting film formed by inhibitors. DDBPB, being more hydrophilic, is not effective enough to entrain the water layer from the steel's surface and cover it with the C₁₂ alkyl chain. Moreover, it may not be advantageous to sacrifice the entropy loss for complete adsorption on the metal surface. Instead, one of the cationic centers is expected to be adsorbed on the surface while the other cationic terminal of DDBPB would protrude into the corroding medium, thereby providing minimum coverage to the metal surface. This is in agreement with the magnitude of Log P values predicted for solubility of inhibitors and the order of corrosion inhibition efficiency obtained from all experimental results.

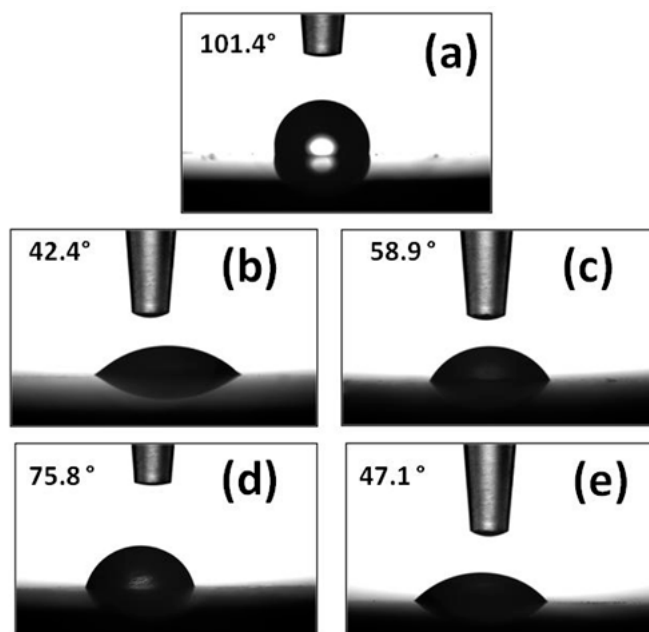


Figure 11. Water droplet images during contact angle measurements of X-60 mild steel in the absence and presence of 30 mg/L inhibitors after complete immersion in 1 M HCl for 24 h at 25 °C; (a) polished X-60 mild steel, (b) X-60 in 1 M HCl in the absence of inhibitor, and X-60 in 1 M HCl in the presence of (c) DDPB, (d) TDPB and (e) DDBPB.

4. Conclusions

Three innovative pyridinium bromide salt derivatives; dodecyl pyridinium bromide (DDPB), tetradecyl pyridinium bromide (TDPB) and dodecyl 1,1'-bispyridinium dibromide (DDBPB) were successfully synthesized, and characterized by the elemental analyzer, FTIR, ¹H-NMR, ¹³C-NMR and surface tensiometer. Evaluations of the corrosion inhibition efficiencies of synthesized compounds were carried out by gravimetric, electrochemical impedance spectroscopy, potentiodynamic polarization and linear polarization measurements. Monte Carlo simulation and partition coefficients (Log P) were used theoretically to predict the electronics and chemical properties of inhibitors on the surface of X-60 mild steel. Surface analysis of the mild steel in the absence and presence of inhibitors was performed with ATR-FTIR, SEM-EDX and contact angle measurements. The following conclusions could be drawn from the results obtained;

1. All synthesized pyridinium bromide salts structures contain a similar π – bond aromatic ring with an electron-rich nitrogen center and a different engineered hydrophobic alkyl chain.
2. Synthesized compounds are promising corrosion inhibitors of mild steel for HCl pickling application at a very low concentration of 30 mg/L. They are potential candidates for the formulation of corrosion inhibitors for industrial applications.
3. The performance of inhibitors is concentration and temperature dependent with the superiority order of TDPB > DDPB > DDBPB.
4. The order of corrosion inhibition efficiencies of synthesized compounds was found not to depend only on the adsorption energy due to similar adsorption centers revealed by Monte Carlo simulation but depend on the hydrophilicity of the inhibitors that formed a protective film on the surface of mild steel.
5. Mixed type corrosion inhibition mechanism of all synthesized compounds was revealed by potentiodynamic polarization resistance.
6. Adsorption of corrosion inhibitors on mild steel was found to obey Langmuir adsorption isotherm despite the major contribution of the film for their efficiencies.

7. Experimental and theoretical results were found to be complementary in understanding the chemical properties of synthesized compounds.

Supplementary Materials: The following are available online at <http://www.mdpi.com/2079-6412/10/2/185/s1>, Figure S1: ¹H NMR spectra of synthesized DDPB (1), TDPB (2) and DDBPB (3) corrosion inhibitors, Figure S2: ¹³C NMR spectra of synthesized DDPB (1), TDPB (2) and DDBPB (3) corrosion inhibitors, Figure S3: FTIR spectra of synthesized DDPB (1), TDPB (2) and DDBPB (3) corrosion inhibitors, Figure S4: Surface tension versus concentration of DDPB, TDPB and DDBPB in 1 M HCl solution at 25 °C, Figure S5: Langmuir adsorption isotherms for DDPB, TDPB and DDBPB on X-60 mild steel in 1 M HCl solution at 25 °C, Figure S6: EDX spectra of X-60 mild steel in absence and presence of 30 mg/L corrosion inhibitors after complete immersion in 1 M HCl for 24 h at 25 °C; (a) Polished X-60 mild steel, (b) X-60 in 1 M HCl in the absence of inhibitor, and X-60 in 1 M HCl in the presence of (c) DDPB, (d) TDPB and (e) DDBPB, Table S1: Surface properties of compounds DDPB, TDPB and DDBPB in 1M HCl solutions at 25 °C., Table S2: Adsorption isotherm of DDPB, TDPB and DDBPB in 1 M HCl on X-60 mild steel at 25 °C.

Author Contributions: Conceptualization, M.A.J.M. and S.A.A.; Methodology, N.A.O., M.A.J.M. and S.A.A.; Validation, A.A.A.-S. and I.B.O.; Formal Analysis, N.A.O. and M.A.J.M.; Investigation, N.A.A. and I.B.O.; Writing—Original Draft Preparation N.A.O. and M.A.J.M.; Writing—Review & Editing, M.A.J.M. and S.A.A.; Funding Acquisition, M.A.J.M., S.A.A., N.A.A. and B.G.A. All authors have read and agreed to the published version of the manuscript.

Funding: Saudi Aramco, Dhahran, Saudi Arabia under a research project # CHEM2414, funded this research.

Acknowledgments: The use of research facilities provided by King Fahd University of Petroleum & Minerals and the financial assistance of Saudi Aramco, Dhahran, Saudi Arabia through project # CHEM2414 is gratefully acknowledged.

Conflicts of Interest: The authors declare no conflict of interest. The funders had no role in the design of the study; in the collection, analyses, or interpretation of data; in the writing of the manuscript, or in the decision to publish the results.

References

1. Guo, Y.; Tan, H.; Meng, T.; Wang, D.; Liu, S. Effects of alternating current interference on the cathodic protection for API 5L X60 pipeline steel. *J. Nat. Gas Sci. Eng.* **2016**, *36*, 414–423. [[CrossRef](#)]
2. Onyeachu, I.B.; Obot, I.B.; Sorour, A.A.; Abdul-Rashid, M.I. Green corrosion inhibitor for oilfield application I: Electrochemical assessment of 2-(2-pyridyl) benzimidazole for API X60 steel under sweet environment in NACE brine ID196. *Corros. Sci.* **2019**, *150*, 183–193. [[CrossRef](#)]
3. Umoren, S.A.; Madhankumar, A. Effect of addition of CeO₂ nanoparticles to pectin as inhibitor of X60 steel corrosion in HCl medium. *J. Mol. Liq.* **2016**, *224*, 72–82. [[CrossRef](#)]
4. Muthukumar, N.; Ilangovan, A.; Maruthamuthu, S.; Palaniswamy, N. Surface analysis of inhibitor films formed by 1-aminoanthraquinones on API 5L-X60 steel in diesel-water mixtures. *Electrochim. Acta* **2007**, *52*, 7183–7192. [[CrossRef](#)]
5. Muthukumar, N.; Ilangovan, A.; Maruthamuthu, S.; Palaniswamy, N.; Kimura, A. 1-Aminoanthraquinone derivatives as a novel corrosion inhibitor for carbon steel API 5L-X60 in white petrol-water mixtures. *Mater. Chem. Phys.* **2009**, *115*, 444–452. [[CrossRef](#)]
6. Guaccia, R.; Randazzo, S.; Chillura Martino, D.; Cipollina, A.; Micale, G. Experimental investigation and modeling of diffusion dialysis for HCL recovery from waste pickling solution. *J. Environ. Manag.* **2019**, *235*, 202–212. [[CrossRef](#)]
7. Xie, Q.; Shi, P.-y.; Liu, C.; Jiang, M.-f. Effects of Different Oxidants on HCL-based Pickling Process of 430 Stainless Steel. *J. Iron Steel Res. Int.* **2016**, *23*, 778–783. [[CrossRef](#)]
8. Odewunmi, N.A.; Umoren, S.A.; Gasem, Z.M.; Ganiyu, S.A.; Muhammad, Q. L-Citrulline: An active corrosion inhibitor component of watermelon rind extract for mild steel in HCL medium. *J. Taiwan Inst. Chem. Eng.* **2015**, *51*, 177–185. [[CrossRef](#)]
9. Sanaei, Z.; Ramezanzadeh, M.; Bahlakeh, G.; Ramezanzadeh, B. Use of Rosa canina fruit extract as a green corrosion inhibitor for mild steel in 1 M HCL solution: A complementary experimental, molecular dynamics and quantum mechanics investigation. *J. Ind. Eng. Chem.* **2019**, *69*, 18–31. [[CrossRef](#)]
10. Mazumder, M.A.J. New, Amino Acid Based Zwitterionic Polymers as Promising Corrosion Inhibitors of Mild Steel in 1 M HCL. *Coatings* **2019**, *9*, 675. [[CrossRef](#)]

11. Wang, W.; Song, Z.; Guo, M.; Jiang, L.; Xiao, B.; Jiang, Q.; Chu, H.; Liu, Y.; Zhang, Y.; Xu, N. Employing ginger extract as an eco-friendly corrosion inhibitor in cementitious materials. *Constr. Build. Mater.* **2019**, *228*, 116713. [[CrossRef](#)]
12. Umoren, S.; Obot, I.B.; Gasem, Z.; Odewunmi, N.A. Experimental and Theoretical Studies of Red Apple Fruit Extract as Green Corrosion Inhibitor for Mild Steel in HCL Solution. *J. Dispers. Sci. Technol.* **2015**, *36*, 789–802. [[CrossRef](#)]
13. Liu, Y.; Song, Z.; Wang, W.; Jiang, L.; Zhang, Y.; Guo, M.; Song, F.; Xu, N. Effect of ginger extract as green inhibitor on chloride-induced corrosion of carbon steel in simulated concrete pore solutions. *J. Clean. Prod.* **2019**, *214*, 298–307. [[CrossRef](#)]
14. Odewunmi, N.A.; Umoren, S.A.; Gasem, Z.M. Journal of Environmental Chemical Engineering Watermelon waste products as green corrosion inhibitors for mild steel in HCL solution. *Biochem. Pharmacol.* **2015**, *3*, 286–296.
15. Nadi, I.; Belattmania, Z.; Sabour, B.; Reani, A.; Sahibed-dine, A.; Jama, C.; Bentiss, F. Sargassum muticum extract based on alginate biopolymer as a new efficient biological corrosion inhibitor for carbon steel in hydrochloric acid pickling environment: Gravimetric, electrochemical and surface studies. *Int. J. Biol. Macromol.* **2019**, *141*, 137–149. [[CrossRef](#)]
16. Odewunmi, N.A.; Umoren, S.A.; Gasem, Z.M. Journal of Industrial and Engineering Chemistry Utilization of watermelon rind extract as a green corrosion inhibitor for mild steel in acidic media. *J. Ind. Eng. Chem.* **2015**, *21*, 239–247. [[CrossRef](#)]
17. Bahlakeh, G.; Ramezanzadeh, B.; Dehghani, A.; Ramezanzadeh, M. Novel cost-effective and high-performance green inhibitor based on aqueous Peganum harmala seed extract for mild steel corrosion in HCL solution: Detailed experimental and electronic/atomic level computational explorations. *J. Mol. Liq.* **2019**, *283*, 174–195. [[CrossRef](#)]
18. Umoren, S.A.; Solomon, M.M.; Obot, I.B.; Suleiman, R.K. A critical review on the recent studies on plant biomaterials as corrosion inhibitors for industrial metals. *J. Ind. Eng. Chem.* **2019**, *76*, 91–115. [[CrossRef](#)]
19. Cao, S.; Liu, D.; Ding, H.; Wang, J.; Lu, H.; Gui, J. Task-specific ionic liquids as corrosion inhibitors on carbon steel in 0.5 M HCL solution: An experimental and theoretical study. *Corros. Sci.* **2019**, *153*, 301–313. [[CrossRef](#)]
20. Yesudass, S.; Olasunkanmi, L.O.; Bahadur, I.; Kabanda, M.M.; Obot, I.B.; Ebenso, E.E. Experimental and theoretical studies on some selected ionic liquids with different cations/anions as corrosion inhibitors for mild steel in acidic medium. *J. Taiwan Inst. Chem. Eng.* **2016**, *64*, 252–268. [[CrossRef](#)]
21. Azeez, F.A.; Al-Rashed, O.A.; Nazeer, A.A. Controlling of mild-steel corrosion in acidic solution using environmentally friendly ionic liquid inhibitors: Effect of alkyl chain. *J. Mol. Liq.* **2018**, *265*, 654–663. [[CrossRef](#)]
22. Sebhaoui, J.; El Bakri, Y.; El Aoufir, Y.; Anouar, E.H.; Guenbour, A.; Nasser, A.A.; Mokhtar Essassi, E. Synthesis, NMR characterization, DFT and anti-corrosion on carbon steel in 1M HCL of two novel 1,5-benzodiazepines. *J. Mol. Struct.* **2019**, *1182*, 123–130. [[CrossRef](#)]
23. Rbaa, M.; Lakhri, B. Novel oxazole and imidazole based on 8-hydroxyquinoline as a corrosion inhibition of mild steel in HCL solution: Insights from experimental and computational studies. *Surf. Interfaces* **2019**, *15*, 43–59. [[CrossRef](#)]
24. Salarvand, Z.; Amirasr, M.; Talebian, M.; Raeissi, K.; Meghdadi, S. Enhanced corrosion resistance of mild steel in 1 M HCL solution by trace amount of 2-phenyl-benzothiazole derivatives: Experimental, quantum chemical calculations and molecular dynamics (MD) simulation studies. *Corros. Sci.* **2017**, *114*, 133–145. [[CrossRef](#)]
25. Luo, X.; Ci, C.; Li, J.; Lin, K.; Du, S.; Zhang, H.; Li, X.; Cheng, Y.F.; Zang, J.; Liu, Y. 4-aminoazobenzene modified natural glucomannan as a green eco-friendly inhibitor for the mild steel in 0.5 M HCL solution. *Corros. Sci.* **2019**, *151*, 132–142. [[CrossRef](#)]
26. Verma, C.; Quraishi, M.A. 2-Amino-3-methyl-3-(4-nitrophenyl)-5-(phenylthio)-3H-pyrrole-4-carbonitrile as effective corrosion inhibitor for mild steel in 1M HCL: Thermodynamical, electrochemical, surface and theoretical calculation. *Ain Shams Eng. J.* **2016**, *7*, 1–9. [[CrossRef](#)]
27. Cherrak, K.; Benhiba, F.; Sebbar, N.K.; Essassi, E.M.; Taleb, M.; Zarrouk, A.; Dafali, A. Corrosion inhibition of mild steel by new Benzothiazine derivative in a hydrochloric acid solution: Experimental evaluation and theoretical calculations. *Chem. Data Collect.* **2019**, *22*, 100252. [[CrossRef](#)]

28. Li, L.; Zhao, Y.; Zhou, H.; Ning, A.; Zhang, F.; Zhao (Kent), Z. Synthesis of pyridinium N-chloramines for antibacterial applications. *Tetrahedron Lett.* **2017**, *58*, 321–325. [[CrossRef](#)]
29. Chen, Y.; Feng, C.; Zhang, Q.; Ren, G.; Han, Q. N-halamine/pyridinium-derivatized magnetic sub-microparticles with synergetic biocidal properties. *Appl. Surf. Sci.* **2019**, *467*, 526–533. [[CrossRef](#)]
30. Omidi, S.; Kakanejadifard, A. Modification of chitosan and chitosan nanoparticle by long chain pyridinium compounds: Synthesis, characterization, antibacterial, and antioxidant activities. *Carbohydr. Polym.* **2019**, *208*, 477–485. [[CrossRef](#)]
31. Hao, J.; Qin, T.; Zhang, Y.; Li, Y.; Zhang, Y. Synthesis, surface properties and antimicrobial performance of novel gemini pyridinium surfactants. *Colloids Surf. B Biointerfaces* **2019**, *181*, 814–821. [[CrossRef](#)] [[PubMed](#)]
32. Moosavi-Zare, A.R.; Zolfigol, M.A.; Salehi-Moratab, R.; Noroozadeh, E. Catalytic application of 1-(carboxymethyl) pyridinium iodide on the synthesis of pyranopyrazole derivatives. *J. Mol. Catal. A Chem.* **2016**, *415*, 144–150. [[CrossRef](#)]
33. Maya, E.M.; Verde-Sesto, E.; Mantione, D.; Iglesias, M.; Mecerreyes, D. New poly (ionic liquid)s based on poly(azomethine-pyridinium) salts and its use as heterogeneous catalysts for CO₂ conversion. *Eur. Polym. J.* **2019**, *110*, 107–113. [[CrossRef](#)]
34. Tankov, I.; Yankova, R. DFT analysis, reaction kinetics and mechanism of esterification using pyridinium nitrate as a green catalyst. *J. Mol. Liq.* **2019**, *277*, 241–253. [[CrossRef](#)]
35. Emmanuel, K.; Erigene, B.; Cheng, C.; Mondal, A.N.; Hossain, M.M.; Khan, M.I.; Afsar, N.U.; Ge, L.; Wu, L.; Xu, T. Facile synthesis of pyridinium functionalized anion exchange membranes for diffusion dialysis application. *Sep. Purif. Technol.* **2016**, *167*, 108–116. [[CrossRef](#)]
36. Qu, S.; Yao, Q.; Wang, L.; Hua, J.; Chen, L. A novel hydrophilic pyridinium salt polymer/SWCNTs composite film for high thermoelectric performance. *Polymer* **2018**, *136*, 149–156. [[CrossRef](#)]
37. Alea-Reyes, M.E.; González, A.; Calpena, A.C.; Ramos-López, D.; de Lapuente, J.; Pérez-García, L. Gemini pyridinium amphiphiles for the synthesis and stabilization of gold nanoparticles for drug delivery. *J. Colloid Interface Sci.* **2017**, *502*, 172–183. [[CrossRef](#)]
38. Ali, S.M.; Emran, K.M.; Messali, M. Improved protection performance of modified sol-gel coatings with pyridinium-based ionic liquid for cast iron corrosion in 0.5 M HCL solution. *Prog. Org. Coat.* **2019**, *130*, 226–234. [[CrossRef](#)]
39. Pohrebkova, I.S.; Pylypenko, T.M. Inhibitors for acid corrosion of metals based on quaternary pyridinium salts containing carbonyl groups. *Mater. Today* **2019**, *6*, 192–201. [[CrossRef](#)]
40. Migahed, M.A. Electrochemical investigation of the corrosion behaviour of mild steel in 2 M HCL solution in presence of 1-dodecyl-4-methoxy pyridinium bromide. *Mater. Chem. Phys.* **2005**, *93*, 48–53. [[CrossRef](#)]
41. Gu, T.; Chen, Z.; Jiang, X.; Zhou, L.; Liao, Y.; Duan, M.; Wang, H.; Pu, Q. Synthesis and inhibition of N-alkyl-2-(4-hydroxybut-2-ynyl) pyridinium bromide for mild steel in acid solution: Box-Behnken design optimization and mechanism probe. *Corros. Sci.* **2015**, *90*, 118–132. [[CrossRef](#)]
42. Xia, G.; Jiang, X.; Zhou, L.; Liao, Y.; Duan, M.; Wang, H.; Pu, Q.; Zhou, J. Synergic effect of methyl acrylate and N-cetylpyridinium bromide in N-cetyl-3-(2-methoxycarbonylvinyl)pyridinium bromide molecule for X70 steel protection. *Corros. Sci.* **2015**, *94*, 224–236. [[CrossRef](#)]
43. Saleh, M.M.; Mahmoud, M.G.; Abd El-Lateef, H.M. Comparative study of synergistic inhibition of mild steel and pure iron by 1-hexadecylpyridinium chloride and bromide ions. *Corros. Sci.* **2019**, *154*, 70–79. [[CrossRef](#)]
44. Shalabi, K.; Helmy, A.M.; El-Askalany, A.H.; Shahba, M.M. New pyridinium bromide mono-cationic surfactant as corrosion inhibitor for carbon steel during chemical cleaning: Experimental and theoretical studies. *J. Mol. Liq.* **2019**, *293*, 111480. [[CrossRef](#)]
45. Cornellas, A.; Perez, L.; Comelles, F.; Ribosa, I.; Manresa, A.; Garcia, T.T. Self-aggregation and antimicrobial activity of imidazolium and pyridinium based ionic liquids in aqueous solution. *J. Colloid Interface Sci.* **2011**, *355*, 164–171. [[CrossRef](#)]
46. Mazumder, M.A.J.; Al-Muallem, H.A.; Ali, S.A. The effects of N-pendants and electron-rich amidine motifs in 2-(p-alkoxyphenyl)-2-imidazolines on mild steel corrosion in CO₂-saturated 0.5M NaCl. *Corros. Sci.* **2015**, *90*, 54–68. [[CrossRef](#)]
47. ASTM G1 Standard Practice for Preparing, Cleaning, and Evaluating Corrosion Test. *Specimens* **1999**, *G1-90*, 15–21.

48. Alhaffar, M.T.; Umoren, S.A.; Obot, I.B.; Ali, S.A. Isoxazolidine derivatives as corrosion inhibitors for low carbon steel in HCl solution: Experimental, theoretical and effect of KI studies. *RSC Adv.* **2018**, *8*, 1764–1777. [[CrossRef](#)]
49. Bajpai, D.; Tyagi, V.K. Fatty imidazolines: Chemistry, synthesis, properties and their industrial application. *J. Oleo. Sci.* **2006**, *55*, 319–329. [[CrossRef](#)]
50. Beverskog, B.; Bojinov, M.; Englund, A.; Kinnunen, P.; Laitinen, T.; Mäkelä, K.; Saario, T.; Sirkiä, P. A mixed-conduction model for oxide films on Fe, Cr and Fe-Cr alloys in high-temperature aqueous electrolytes-I. Comparison of the electrochemical behaviour at room temperature and at 200 °C. *Corros. Sci.* **2002**, *44*, 1901–1921. [[CrossRef](#)]
51. Khanra, A.; Gayen, R.N. Distribution of relaxation time in solution-processed polycrystalline CZTS thin films: Study of impedance spectroscopy. *Ceram. Int.* **2018**, *44*, 14095–14100. [[CrossRef](#)]
52. Carranza, R.M.; Alvarez, M.G. The effect of temperature on the passive film properties and pitting behaviour of a Fe-Cr-Ni alloy. *Corros. Sci.* **1996**, *38*, 909–925. [[CrossRef](#)]
53. Solomon, M.M.; Umoren, S.A.; Quraishi, M.A.; Jafar Mazumder, M.A. Corrosion inhibition of N80 steel in simulated acidizing environment by N-(2-(2-pentadecyl-4,5-dihydro-1H-imidazol-1-yl) ethyl) palmitamide. *J. Mol. Liq.* **2019**, *273*, 476–487. [[CrossRef](#)]
54. Roy, P.; Pal, A.; Sukul, D. Origin of the synergistic effect between polysaccharide and thiourea towards adsorption and corrosion inhibition for mild steel in sulphuric acid. *RSC Adv.* **2014**, *4*, 10607–10613. [[CrossRef](#)]
55. Lozano, I.; Mazario, E.; Olivares-Xometl, C.O.; Likhanova, N.V.; Herrasti, P. Corrosion behaviour of API 5LX52 steel in HCL and H₂SO₄ media in the presence of 1,3-dibencilimidazolio acetate and 1,3-dibencilimidazolio dodecanoate ionic liquids as inhibitors. *Mater. Chem. Phys.* **2014**, *147*, 191–197. [[CrossRef](#)]
56. Obot, I.B.; Kaya, S.; Kaya, C.; Tüzün, B. Theoretical evaluation of triazine derivatives as steel corrosion inhibitors: DFT and Monte Carlo simulation approaches. *Res. Chem. Intermed.* **2016**, *42*, 4963–4983. [[CrossRef](#)]
57. Obot, I.B.; Solomon, M.M.; Umoren, S.A.; Suleiman, R.; Elanany, M.; Alanazi, N.M.; Sorour, A.A. Progress in the development of sour corrosion inhibitors: Past, present, and future perspectives. *J. Ind. Eng. Chem.* **2019**, *79*, 1–18. [[CrossRef](#)]
58. Zhu, Y.; Free, M.L.; Woollam, R.; Durnie, W. A review of surfactants as corrosion inhibitors and associated modeling. *Prog. Mater. Sci.* **2017**, *90*, 159–223. [[CrossRef](#)]



© 2020 by the authors. Licensee MDPI, Basel, Switzerland. This article is an open access article distributed under the terms and conditions of the Creative Commons Attribution (CC BY) license (<http://creativecommons.org/licenses/by/4.0/>).